

Chiral molecules and magnets as efficient thermoelectric convertersDan Klein  and Karen Michaeli*Department of Condensed Matter Physics, Weizmann Institute of Science, Rehovot 7630031, Israel*

(Received 22 January 2023; revised 15 June 2023; accepted 20 June 2023; published 10 August 2023)

Thermoelectric effects allow replacing mechanical work with electric power, and the resulting devices can be used as heat engines or refrigerators. In the former, a voltage is generated by connecting the device to contacts at different temperatures, while in the latter electric power induces the heat flow from cold to hot reservoirs. Thermoelectric nanoscale devices hold great technological potential due to the ability to integrate them into chips. So far, however, their practical use is hindered by their low performance. We suggest here a design for thermoelectric devices based on chiral organic molecules connected to two magnetic electrodes. Our device utilizes the chiral-induced spin selectivity exhibited by such chiral systems and specifically its main manifestation of strong spin-dependent transport. We analyze the figure of merit and generated power of chiral-molecule-based heat engines and show that both can be significant with the potential to exceed other existing designs.

DOI: [10.1103/PhysRevB.108.075407](https://doi.org/10.1103/PhysRevB.108.075407)**I. INTRODUCTION**

Recent years have brought the discovery of various spin-dependent effects in chiral organic molecules and structures. All these phenomena, which are of the same origin, reside under the umbrella of chirality-induced spin selectivity (CISS). Two basic experimental observations of CISS include strong spin-dependent scattering through self-assembled monolayers of chiral molecules [1–3] and large asymmetric magnetoresistance of single molecules [3–5]. Other signatures of CISS, extending beyond transport phenomena, include nontrivial interaction with magnetic substrates, such as handedness-dependent adsorption time [6] and significant transient spin torque [7]. Theory suggests that CISS stems from a combination of the molecules' geometry, spin-orbit coupling (SOC), and strong electron-phonon interactions. The first two elements are essential to endow spin dependence [8–16], while the interactions sustain the effect at room temperature. Understanding the mechanism leading to CISS is a matter of importance for basic biological processes such as photosynthesis and respiration. Apart from its fundamental aspects, there are various suggestions for CISS-based applications. For example, chiral organic molecules can be used instead of ferromagnetic electrodes for spin injection purposes [17] or for manipulation of magnetic memory [18,19]. Alternatively, magnets can be used to purify a racemic mixture of artificially synthesized molecules [6].

The aim of this paper is to explore a new field where CISS holds potential for great improvement: thermoelectric engines and refrigerators based on chiral molecules and magnets. As climate change becomes an issue of critical importance to humanity, the race for efficient generation of electricity and alternative sources of energy increases in urgency. In 2020, in the United Kingdom, for example, Fenwick and Jones cited thermoelectric conversion as one of five pathways to reaching zero net emissions of CO₂ by the year 2050 [20]. The reliability of thermoelectric devices is superior compared to their mechanical counterparts, making them prime candidates

for robust technological applications. For example, typical household refrigerators or CPU coolers have moving parts that can malfunction over time due to degradation, unlike their thermoelectric implementation [21]. So far, however, the practical use of thermoelectric devices is hindered by their poor performance. Current applications include stabilizing laser wavelengths by maintaining a constant temperature and climate-control seat systems that increase passenger comfort in vehicles [22]. Nanoscale thermoelectric devices are of special interest as they hold potential for integration on chips. On a more fundamental level, such thermoelectric devices constitute simple quantum machines where thermodynamics and quantum mechanics must be treated in a unified manner.

The quality of thermoelectric machines is usually characterized by their maximal efficiency and their efficiency at maximal power. The efficiency of a heat engine is determined by the ratio of work it produces to the thermal current flowing out of the hot contact. The latter describes the heat flux that needs to be externally supplied to the device to maintain the temperature difference between the contacts. The efficiency of a thermoelectric refrigerator is given by the inverse ratio. In the regime of linear response, the efficiency of thermoelectric machines is usually determined by a single material parameter, the dimensionless figure of merit, $ZT = \alpha \Pi / RK$. Here R and K^{-1} are the electrical and thermal resistances. The Seebeck and Peltier coefficients, α and Π , describe the thermoelectric effects, and T is the reference temperature for linear response. In time-reversal-symmetric systems, Onsager's relations impose the constraint $\Pi = \alpha T$. This reduces the number of transport coefficients that determine the efficiency to three. Specifically, the maximum efficiency of a heat engine working between two temperatures T_{high} and T_{low} ,

$$\eta_{\text{max}} = \eta_C \frac{\sqrt{1 + ZT} - 1}{\sqrt{1 + ZT} + 1}, \quad (1)$$

depends solely and monotonously on the figure of merit, ZT . The Carnot efficiency $\eta_C = 1 - T_{\text{low}}/T_{\text{high}}$ is attained in the

limit $ZT \rightarrow \infty$. In this limit, the rate of entropy production, the produced power, and the thermal current *all* vanish. Similarly to η_{\max} , the efficiency at maximal power also increases with ZT . Common wisdom states that a practical thermoelectric engine should have $ZT \gtrsim 3$ [22].

The quest for better bulk thermoelectric materials is ongoing and has expanded from semiconductors to include Heusler alloys [23], half-Heusler alloys [24], and topological insulators [25], reaching values of $ZT \gtrsim 10$ under certain conditions. The performance of such solutions in *ambient conditions* is more modest, however, and is sensitive to fabrication conditions. Thus, simple mass production of highly efficient thermoelectric devices is still out of reach. Nanoscale and mesoscale thermoelectric devices currently exist only on a theoretical level. Mahan and Sofo [26] showed that transmission through resonance levels can maximize the figure of merit, a concept that several works have since echoed [27,28]. As expected, operating at Carnot efficiency comes at the price of vanishing power production, rendering such engines impractical and necessitating more delicate optimization. In the absence of interactions, the Wiedemann-Franz law, the Mott formula for the thermopower [29], and Onsager relation in the absence of external fields strongly constrain the paths to optimize ZT . Specifically, all transport coefficients entering the figure of merit are proportional to the transmission probability of the free electron system. One way of breaching these limitations is through the application of an external magnetic field \mathbf{B} . The more relaxed Onsager-Casimir [30] relation $\alpha(-\mathbf{B})T = \Pi(\mathbf{B})$ allows, in principle, for $\alpha(\mathbf{B})T \neq \Pi(\mathbf{B})$, thus increasing the parameter space [31]. In systems where the two thermoelectric coefficients strongly differ, high efficiency is attainable at near-Carnot efficiency, without the need for an infinite figure of merit. Theoretical models realizing $\alpha(\mathbf{B})T \neq \Pi(\mathbf{B})$ exhibit potential for better performance [31–36], but require operating at low temperatures and high magnetic fields. Other theoretical proposals [37–39] explore the idea of realizing thermoelectric devices using systems where both quantum effects and interactions play a significant role.

We suggest here using chiral organic molecules exhibiting CISS as building blocks for efficient thermoelectric nanoscale devices. The spin-dependent transport properties of these systems are prominent at room temperature, and their natural self-assembly on surfaces makes them easy to fabricate. The strong asymmetry in magnetoresistance, which occurs upon coupling chiral molecules to a weak magnet, suggests that the constraint $\alpha(\mathbf{B})T = \Pi(\mathbf{B})$ also breaks under the same condition. The asymmetry in the magnetoresistance and in the thermoelectric transport coefficients is only possible due to strong interactions [40]. Various works [41–45] have pointed to electron-phonon interactions as crucial for enhancing the spin-dependent effects as well as giving rise to the robust signature of CISS in transport. In particular, we have analyzed [46] the role of polarons in enhancing the manifestation of CISS in both scattering and magnetoresistance experiments.

Here we propose a design for a thermoelectric engine based on chiral molecules connected to two magnetic electrodes. The two leads are magnetized in an opposite direction and, hence, electron transfer must involve a spin flip. The latter is achieved through the mechanism that generates CISS: an

electron moving along a chiral structure gets spin polarized in the presence of SOC [47]. Specifically, for chiral organic molecules, the bare effect of the SOC is small and becomes significant only when accompanied by the absorption or emission of phonons. As a result, the figure of merit is only weakly tied to the electronic spectrum, via the magnitude of the SOC. Rather, it is predominantly a function of the phononic density of states and the strength of the electron-phonon coupling. Thus, our device utilizes the combined effect of strong electron-phonon interactions and CISS. By contrast, it does not rely on the asymmetry between the Peltier and the Seebeck coefficients. Calculating the deviation of the ratio $\alpha(\mathbf{B})T/\Pi(\mathbf{B})$ from unity, and designing a thermoelectric device that exploits it, is beyond the scope of this paper.

Our proposal echoes the results of a previous work by Jiang and co-workers [38] (referred to as JEWI below). They were the first to show the enhancement in thermoelectric efficiency due to phonon-assisted transport. JEWI analyzed the figure of merit of a thermoelectric engine based on a semiconducting *n-i-p* junction. In their proposal, particle current is generated in the intrinsic region by phonons creating electron-hole pairs. Thus, the heat from the phononic bath is converted into electrical power. Contrary to the suggestion of Mahan and Sofo [26], where a small bandwidth for elastic transport was key to enhancing thermoelectric conversion, in JEWI's device the figure of merit benefits from a low effective *phonon bandwidth*. In this paper, we show the additional benefit of a thermoelectric device based on the CISS effect. We first perform a general analysis using a toy model of our proposed device. We then calculate, using a diagrammatic approach, the linear transport coefficients of chiral molecules.

The remainder of the paper is organized as follows. In the next section, we discuss the general properties of three-terminal machines comprised of two electron electrodes and one phonon bath. In Sec. III we present a model for transport through a chiral molecule connected to two oppositely magnetized electrodes. In Sec. IV we present the framework for the calculation of transport coefficients. In Secs. V and VI we study the efficiency and power production of the chiral-molecule-based thermoelectric device using the proposed model. We conclude in Sec. VII.

II. GENERAL PROPERTIES OF THREE TERMINAL DEVICES

Our proposed thermoelectric device is built from a chiral molecule connected to two electrodes. Inside the molecule, electrons interact strongly with phonons. Such a setup is equivalent to a three-terminal device coupled to two electron baths and one phonon bath. The electron baths define the temperature $T_i = \beta_i^{-1}$ and chemical potential μ_i at the two ends of the molecule, $i = L, R$. The phonon bath introduces a third temperature $T_{\text{ph}} = \beta_{\text{ph}}^{-1}$ in the middle of the molecule. The three-terminal device can operate in refrigeration or heat engine modes. In the former, the temperature of the phonon bath is lower than that of the electronic leads, and energy is removed from it by applying a voltage between the electrodes. In the latter, the temperature of the phonon bath is higher than that of the electronic leads, and the resulting electric current flowing between the electrodes generates electrical power.

According to the second law of thermodynamics, the non-negativity of the sum of entropy productions in the reservoirs $\dot{S}_{L/R/ph}$ reads

$$0 \leq \dot{S}_L + \dot{S}_R + \dot{S}_{ph} = -J_L^{th}\beta_L - J_R^{th}\beta_R - J_{ph}^{th}\beta_{ph}. \quad (2)$$

The thermal currents going into the reservoirs, J_i^{th} , which are by definition proportional to the flow of entropy, can be extracted from the free energy. Thus, the thermal current out of reservoir i is defined as $J_i^{th} = J_i^e - \mu_i J_i^c/e$, where J_i^e and J_i^c are the energy and charge currents, respectively. For the phonons, the chemical potential is zero. Equation (2) can be simplified by using the charge and energy conservation laws

$$J_L^e + J_R^e = 0, \quad (3a)$$

$$J_L^e + J_R^e + J_{ph}^e = 0. \quad (3b)$$

The redundancy implied by these conservation laws allows us to consider only three currents. We choose to study the electric and thermal currents out of the left electronic reservoir, J_L^e and J_L^{th} , as well as the thermal current out of the phonon bath $J_{ph}^{th} = J_{ph}^e$. Writing the entropy production rate in terms of these currents yields

$$0 \leq \dot{S}_L + \dot{S}_R + \dot{S}_{ph} = -J_L^{th}(\beta_L - \beta_R) - J_{ph}^{th}(\beta_{ph} - \beta_R) + J_L^e \beta_R \frac{\mu_L - \mu_R}{e}. \quad (4)$$

The above expression for the entropy production rate helps us identify the driving forces for the three currents: $-\Delta\beta_L = -(\beta_L - \beta_R)$, $-\Delta\beta_{ph} = -(\beta_{ph} - \beta_R)$, and $\Delta\mu = \mu_L - \mu_R$. The forces define the conductivity matrix in the regime of linear response,

$$\begin{pmatrix} J_L^e \\ J_L^{th} \\ J_{ph}^{th} \end{pmatrix} = L \begin{pmatrix} \Delta\mu/e \\ -\Delta\beta_L \\ -\Delta\beta_{ph} \end{pmatrix}, \quad (5)$$

with

$$L = \begin{pmatrix} G & \alpha_e & \alpha_{ph} \\ \beta_R \Pi_e & \kappa_{LR} & \kappa_{L,ph} \\ \beta_R \Pi_{ph} & \kappa_{ph,L} & \kappa_{ph} \end{pmatrix}. \quad (6)$$

Here G , α_e , Π_e , and κ_{LR} are the direct electronic contributions to the electric conductance, thermopower (Seebeck coefficient), Peltier coefficient, and the thermal conductivity, respectively. The contributions due to the coupling of electrons with the vibrational modes are α_{ph} , Π_{ph} , $\kappa_{L,ph}$, and $\kappa_{ph,L}$. Finally, κ_{ph} is the direct contribution of the phononic modes to the thermal current. The matrix L satisfies Onsager-Casimir relations [30,48], $L_{ij}(\mathbf{B}) = L_{ji}(-\mathbf{B})$ when an external magnetic field \mathbf{B} is applied. Notice that the form of the conductivity matrix is not unique. An alternative choice of currents, for example, replacing J_{ph}^{th} by J_R^{th} , would result in a different set of driving forces and a different conductivity matrix. Regardless of the choice of currents, correctly identifying the corresponding driving forces (from the second law of thermodynamics) guarantees that the Onsager-Casimir relations hold [49].

We use the above conductivity matrix for the three-terminal setup to analyze the performance of our chiral-molecule-based thermoelectric device. We separate the calculation into

two steps. First, we show the advantage of limiting the number of states through which phonon-assisted electron conduction can occur. In particular, we find the figure of merit and power production as a function of the density of states available for charge transfer. We use a simple toy model that provides important insight into the dominant scales in the problem. Then, we replace the toy model with a microscopic effective model of chiral molecule exhibiting CISS.

III. TOY MODEL

We start our analysis of the CISS-based thermoelectric device by considering a simple model consisting of a molecular chain bridging between two electrodes. The left and right leads are governed by a uniform nearest-neighbor hopping Hamiltonian, i.e.,

$$\mathcal{H}_{L/R} = -\zeta \sum_{n=1}^{\infty} \sum_s [d_{L/R,n+1,s}^\dagger d_{L/R,n,s} + \text{H.c.}]. \quad (7)$$

The operator $d_{L/R,n,s}^\dagger$ ($d_{L/R,n,s}$) creates (annihilates) an electron in state s on site n of lead L or R. The left lead is realized by a p -type semiconductor and the right lead by an n -type semiconductor. The total Hamiltonian is

$$\mathcal{H}_{\text{tot}} = \mathcal{H}_L + \mathcal{H}_{\text{mol}} + \mathcal{H}_R + \sum_s [\gamma_s^L c_{1,s}^\dagger d_{L,1,s} + \gamma_s^R c_{N,s}^\dagger d_{R,1,s} + \text{H.c.}]. \quad (8)$$

The operator $c_{n,s}^\dagger$ ($c_{n,s}$) creates (annihilates) an electron of spin s on site n inside the chain $1 < n < N$. The parameter γ_s^i is the coupling of the molecule to lead i . The index s allows the implementation of a magnetic lead where the coupling is spin dependent. Each site of the molecular chain hosts a single electronic state per site and is coupled to a phonon bath:

$$\mathcal{H}_{\text{mol}} = \sum_{n,s} \tilde{t} [c_{n,s}^\dagger c_{n+1,s} + c_{n+1,s}^\dagger c_{n,s}] + \sum_{q,n} \Omega_q a_{q,n}^\dagger a_{q,n} + \sum_{n,q,s} M_q c_{n,s}^\dagger c_{n,s} (a_{q,n}^\dagger + a_{q,n}). \quad (9)$$

The first term describes nearest-neighbor hopping. We model the phonon bath as a set of optical vibrational modes [50]; the operator $a_{q,n}^\dagger$ ($a_{q,n}$) creates (annihilates) a phonon of frequency Ω_q on site n , and M_q is the coupling constant between the electrons and the environment.

In the strong-coupling limit, polarons are the natural quasiparticles of the system [51,52]. The Lang-Firsov transformation

$$c_n \rightarrow e^S c_n e^{-S} \equiv c_n X_n, \quad (10a)$$

$$S = \sum_{n,q,s} \frac{M_q}{\Omega_q} c_{n,s}^\dagger c_{n,s} (a_{q,n}^\dagger - a_{q,n}), \quad (10b)$$

transforms the Hamiltonian into the polaron basis. Consequently, the molecule's Hamiltonian, Eq. (9), becomes

$$\begin{aligned} \tilde{\mathcal{H}}_{\text{mol}} &= e^S \mathcal{H}_{\text{mol}} e^{-S} = -U \sum_{n,s} c_{n,s}^\dagger c_{n,s} \\ &+ \sum_q \Omega_q a_q^\dagger a_q + \tilde{t} \sum_{s,n} [\lambda_{n+1,n} c_{n,s}^\dagger c_{n+1,s} + \text{H.c.}] \\ &+ \tilde{t} \sum_{s,n} [(X_n^\dagger X_{n+1} - \lambda_{n+1,n}) c_{n,s}^\dagger c_{n+1,s} + \text{H.c.}]. \quad (11) \end{aligned}$$

The operator X_n (X_n^\dagger) annihilates (creates) the phonons' cloud accompanying the electrons, where $X_n = \exp\{\sum_{q,s} M_q(a_{q,n} - a_{q,n}^\dagger)/\Omega_q\}$. In the absence of electrons, the average phononic cloud's fluctuations are given by $\lambda_{n,n+1} \equiv \lambda = \langle X_{n+1}^\dagger X_n \rangle < 1$ and $U = \sum_q \frac{M_q^2}{\Omega_q}$ is the corresponding polaron shift. The last term in $\tilde{\mathcal{H}}_{\text{mol}}$ corresponds to the phonon cloud rearranging in conjunction with a hopping event, beyond its mean-field state. We neglect here the phonon-mediated electron-electron interaction term, which is induced by the transformation. Since we are interested in transport through states residing in the band gap, few electrons participate and their interactions are negligible.

We consider here the effect of polaron fluctuations on the thermoelectric transport properties beyond mean-field effects. While mean-field theory only narrows the polaron bandwidth by suppressing the hopping amplitude $t = \tilde{t}\lambda$, fluctuations allow for phonon-assisted polaron hopping between sites. Nevertheless, the band narrowing plays an important role in our model—we study the role of bandwidth Ω in improving the efficiency of our thermoelectric device. In our setup, the top of the valence band of the left lead (p -type semiconductor) resides below the conduction band of the molecule; the energy gap between the two bands is denoted by the parameter Δ . By contrast, the conduction band of the molecule overlaps that of the right lead (n -type semiconductor). Consequently, a polaron can transfer between the leads only by emitting or absorbing phonons. Specifically, an incoming electron that does not interact with the phonons cannot contribute to any current due to the mismatch between the density of states in the leads. See Fig. 1 for an illustration of the setup and the energy scales in the problem.

An important ingredient of the engine is the suppression of elastic transport, similar to the work of JEWI. This is achieved by sandwiching the molecular chain between n - and p -type semiconductors; i.e., an electron must change its energy while transferring between the leads. This energy adjustment is achieved by phonon absorption or emission.

IV. CALCULATION OF THE TRANSPORT COEFFICIENTS

The electric and heat currents through a system coupled to two leads are given by the Landauer formula in the absence of interactions. Meir and Wingreen [53] have generalized Landauer's expression to interacting systems. Their expressions for the currents are written in terms of the many-body Green's function (GF). Specifically, the current into the lead j is

$$J_j^{\text{e,th}} = \frac{ie}{\hbar} \int d\varepsilon \sum_{\mathbf{n},\mathbf{n}'} \eta_\varepsilon \Gamma_{\mathbf{n}',\mathbf{n}}^j \{G_{\mathbf{n},\mathbf{n}'}^<(\varepsilon)[1 - f_j(\varepsilon)] + G_{\mathbf{n},\mathbf{n}'}^>(\varepsilon)f_j(\varepsilon)\}. \quad (12)$$

The parameter η_ε equals e for the electric current and $\varepsilon - \mu_j$ for the thermal current. Here $G_{\mathbf{n}',\mathbf{n}}$ is the fully dressed Keldysh GF [54], and $<$ and $>$ denote its lesser and greater components. To ease notation, we combine indices into bold notation, $\mathbf{n} = n, s$. The bare (noninteracting) current vertex of lead j is $\Gamma_{\mathbf{n}',\mathbf{n}}^j = 2\pi \rho_s^j \delta_{s,s'} \delta_{n,j} \delta_{n',j}$, and $f_j(\varepsilon)$ is the Fermi-Dirac distribution function of the same lead. The parameter

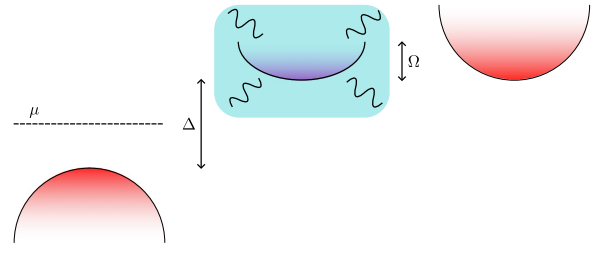


FIG. 1. Illustration of the toy-model-based thermoelectric device. The figure shows the position in energy of the electronic bands of the leads (red) and the molecular chain connecting them (pink). The chemical potential is in the middle between the conduction and the valence bands of the right and left leads, respectively. The narrow window for transport (Ω , the “molecule”) fully overlaps with the conduction band of the right lead, and is at energy Δ above the valence band of the left lead. The turquoise rectangle and wavy lines symbolize the phonon environment.

$\rho_s^j(\varepsilon)$ is the density of states in the lead j per spin s at energy ε , which is also a function of the parameters γ_s^j appearing in the Hamiltonian.

We calculate the current perturbatively, keeping terms up to second order in the electron-phonon coupling. Hence, the Green's function $G_{\mathbf{n}',\mathbf{n}}$ is approximated to be

$$G^{R,A} = g^{R,A} + g^{R,A} \cdot \Sigma^{R,A} \cdot g^{R,A}. \quad (13)$$

The bare Green's function and the self-energy are

$$g^{R,A} = \left[\varepsilon - H_{\text{sub}}^{\text{el}} \pm \frac{i}{2} [\Gamma^L + \Gamma^R] \right]^{-1}, \quad (14a)$$

$$\Sigma_{\mathbf{n},\mathbf{n}'}^{R,A}(\varepsilon) = i \sum_{q,p,p'} \int \frac{d\omega}{2\pi} [D_{n,p;p',n'}^>(q, \omega) g_{\mathbf{p},\mathbf{p}'}^{R,A}(\varepsilon - \omega) + D_{n,p;p',n'}^{R,A}(q, \omega) g_{\mathbf{p},\mathbf{p}'}^<(\varepsilon - \omega)], \quad (14b)$$

where the Hamiltonian $H_{\text{sub}}^{\text{el}}$ describes the electrons of the finite subsystem within the polaron mean-field approximation, i.e., in the absence of phonon fluctuations. The propagation of the phonon cloud can be written as $D_{n,p;p',n'}(q, \omega) = V_{n,p} U_{n,p;p',n'}(q, \omega) V_{p',n'}$. The matrix $V_{n,p} = t[\delta_{n,p-1} + \delta_{n,p+1}]$ appears because the polaron fluctuation terms are nondiagonal in the coordinate. The function $U_{n,p;p',n'} = -i[\langle T[X_n^\dagger(t)X_p(t)X_{p'}^\dagger(0)X_{n'}(0)] - \lambda^2 \rangle]$ is the (time-ordered) four-point correlation function of the phonon cloud. An additional simplification of the propagator is obtained by neglecting the renormalization of the phonon modes by the electrons. Such a scenario occurs for a large boson bath, i.e., in the presence of a large number of phonons, as we expect to have in organic molecules. Consequently, the correlation function of the phonon cloud maintains a simple form:

$$U_{n,p;p',n'}^{R,A}(q, \omega) = 2\lambda^2 \sum_{m=1}^{\infty} \left[\frac{1}{\omega - m\Omega_q \pm i\delta} - \frac{1}{\omega + m\Omega_q \pm i\delta} \right] \times [I_m(-y)|\delta_{n,p'} - \delta_{n',p}| + I_m(y)|\delta_{n,n'} - \delta_{p,p'}| + I_m(-2y)\delta_{n,p'}\delta_{n',p} + I_m(2y)\delta_{n,n'}\delta_{p,p'}] \times \sinh\left(\frac{m\Omega_q}{2T}\right). \quad (15)$$

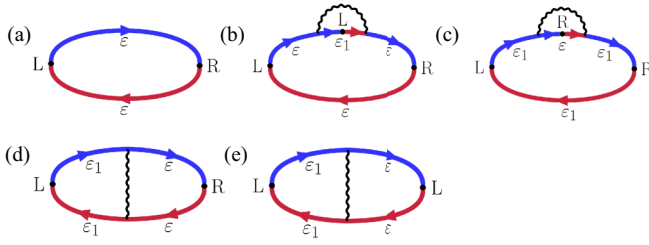


FIG. 2. Diagrammatic representation of contributions to the transport coefficients appearing in Eq. (6). The curved lines are the bare electronic Green's function. We use the color code to indicate the retarded (blue) and advanced (red) GFs. The indices L and R denote the lead from which the GFs end or start, and $\varepsilon_1 = \varepsilon - \omega$. The wavy line represents the combination $D^R - D^A$. The nointeracting bubble (a), corrections to the polaronic Green's function [(b) and (c)], and vertex corrections, one describing passage along the molecule (d) and one describing reflection (e). Feynman diagrams are drawn using TikZ-Feynman [55].

The index m counts the number of excitations in the cloud, and $I_m(y)$ is the modified Bessel function of order m with $y^{-1} = (\omega_q/M_q)^2 \sinh(\omega_q/2T)$. The lesser and greater components of the bosonic propagator are $D^<(\omega) = N(\omega)[D^R(\omega) - D^A(\omega)]$ and $D^>(\omega) = [1 + N(\omega)][D^R(\omega) - D^A(\omega)]$, where $N(\omega)$ is the Bose-Einstein distribution.

Similarly, we can find the lesser and greater components of the polaron's Keldysh GF to the same order:

$$G^< = i \sum_{j=L,R} f_j [g^R \cdot \Gamma^j \cdot g^A + g^R \cdot \Sigma^R \cdot g^R \cdot \Gamma^j \cdot g^A + g^R \cdot \Gamma^j \cdot g^A \cdot \Sigma^A \cdot g^A] + g^R \cdot \Sigma^< \cdot g^A, \quad (16a)$$

$$\Sigma_{\mathbf{n},\mathbf{n}'}^<(\varepsilon) = i \sum_{q,p,p'} \int \frac{d\omega}{2\pi} D_{n,p,p',n'}^<(\vec{k}, \omega) g_{\mathbf{p},\mathbf{p}'}^<(\varepsilon - \omega). \quad (16b)$$

To simplify notation, we use dots to denote the product of matrices, i.e., $[A \cdot B]_{\mathbf{n},\mathbf{n}'}^\varepsilon = \sum_{\mathbf{p}} A_{\mathbf{n},\mathbf{p}}(\varepsilon) B_{\mathbf{p},\mathbf{n}'}(\varepsilon)$. To find $G^>(\varepsilon)$ we exchange between the lesser and greater indices and replace the distribution function by $-1 + f_j$. See Ref. [46] for a detailed derivation of the self-energy.

The expressions for the various components of the Keldysh Green's function and self-energy allow us to write the electric and heat currents up to second order in the electron-phonon coupling using its diagrammatic representation (Fig. 2):

$$\begin{aligned} J_L^{\text{e,th}} = & -\frac{1}{\hbar} \int \frac{d\varepsilon}{2\pi} \eta_\varepsilon \mathcal{I}_a [f_R^\varepsilon - f_L^\varepsilon] - \frac{1}{2\hbar} \int \frac{d\varepsilon d\omega}{(2\pi)^2} \\ & \times [\eta_\varepsilon \mathcal{I}_b + \eta_{\varepsilon-\omega} \mathcal{I}_c + 2i\eta_{\varepsilon-\omega} \mathcal{I}_d] [f_R^\varepsilon - f_L^{\varepsilon-\omega}] \\ & \times [N_\omega^{\text{ph}} - N_\omega^{\text{mix}}] + \frac{1}{2\hbar} \int \frac{d\varepsilon d\omega}{(2\pi)^2} [\eta_\varepsilon \mathcal{I}_b - 2i\eta_{\varepsilon-\omega} \mathcal{I}_e] \\ & \times [f_L^\varepsilon - f_L^{\varepsilon-\omega}] [N_\omega^{\text{ph}} - N_\omega^{\text{L}}] + \frac{1}{2\hbar} \int \frac{d\varepsilon d\omega}{(2\pi)^2} \eta_{\varepsilon-\omega} \mathcal{I}_c \\ & \times [f_R^\varepsilon - f_R^{\varepsilon-\omega}] [N_\omega^{\text{ph}} - N_\omega^{\text{R}}]. \end{aligned} \quad (17)$$

Here, \mathcal{I}_α refers to the product of electron and phonon GFs as indicated by diagram α . The explicit expressions for these functions are given in Appendix A. The temperature entering the Fermi-Dirac distribution function of the left (right) lead

is always T_L (T_R). The Bose-Einstein distribution functions N^j can, on the other hand, depend on the temperature of either the leads $j = L/R$ or the phonons N^{ph} . In addition, we use the shorthand notation $N_\omega^{\text{mix}} = N[(\varepsilon - \mu_R)/T_R - (\varepsilon - \omega - \mu_L)/T_L]$, which arises from the identity $f_\varepsilon^R (f_{\varepsilon-\omega}^L - 1) = N_\omega^{\text{mix}} (f_\varepsilon^R - f_{\varepsilon-\omega}^L)$. The above expressions for the currents are written for arbitrary temperature difference and voltage. To calculate the transport coefficients, we expand the currents to linear order in the driving fields we indicated previously.

V. CHARACTERISTICS OF THE THERMOELECTRIC DEVICE: TOY MODEL CALCULATION

The toy model described above is constructed to allow only phonon-assisted electron transport between leads at temperatures lower than the band gap $\beta\Delta \gg 1$. An incoming electron that does not interact with the phonons cannot contribute to any current due to the mismatch between the densities of states in the leads. Consequently, out of the different contributions to the current described in Eq. (17) and Fig. 2 only the vertex correction term \mathcal{I}_d is important. In linear response, this contribution becomes

$$J_L^{\text{e,th}} \approx \frac{i}{\beta_R \hbar} \int \frac{d\varepsilon d\omega}{(2\pi)^2} \eta_{\varepsilon-\omega} \mathcal{I}_d [f_R^\varepsilon - f_R^{\varepsilon-\omega}] \frac{\partial N_\omega^{\text{R}}}{\partial \omega} \times [\beta_R \Delta \mu - \Delta \beta_L (\varepsilon - \omega - \mu_R) - \Delta \beta_{\text{ph}} \omega]. \quad (18)$$

To find the various components of the three-terminal conductivity matrix (6), we need to find the thermal current in the phonon bath. For this purpose, we calculate the currents in the right lead and use the conservation laws given in Eq. (3). To find the current in the right lead, we replace the index L with R in the expression for $J_L^{\text{e,th}}$ in Eq. (17). In the regime of linear response, this current becomes

$$J_R^{\text{e,th}} \approx \frac{i}{\beta_R \hbar} \int \frac{d\varepsilon d\omega}{(2\pi)^2} \eta_\varepsilon \bar{\mathcal{I}}_d [f_R^\varepsilon - f_R^{\varepsilon-\omega}] \frac{\partial N_\omega^{\text{R}}}{\partial \omega} \times [-\beta_R \Delta \mu + \Delta \beta_L (\varepsilon - \omega + \mu_R) + \Delta \beta_{\text{ph}} \omega]. \quad (19)$$

$\bar{\mathcal{I}}_d$ is derived from \mathcal{I}_d by replacing the L and R indices and performing the transformation $\varepsilon \rightarrow \varepsilon + \omega$ and $\omega \rightarrow -\omega$.

To further simplify the toy model, we assume the polaron Green's function has two different possible values as a function of energy: it is large for energies inside the conduction band and exponentially suppressed otherwise, i.e.,

$$g_{\mathbf{n},\mathbf{n}'}^{\text{R}}(\varepsilon) = \begin{cases} g_0, & \Delta/2 < \varepsilon < \Delta/2 + \Omega \\ \delta g_0 \ll g_0, & \text{otherwise.} \end{cases} \quad (20)$$

Under these assumptions, the conductivity matrix obtains a simple form

$$\begin{aligned} L_{i,j} = & i \int \frac{d\varepsilon d\omega}{(2\pi)^2} B(\omega) \frac{\partial N_\omega^{\text{R}}}{\partial \omega} \mathcal{L}_{i,j}(\varepsilon, \omega) \Gamma_{\text{R}}^\varepsilon \Gamma_{\text{L}}^{\varepsilon-\omega} \\ & \times [f_{\text{R}}^\varepsilon - f_{\text{R}}^{\varepsilon-\omega}] |g_0|^2 |\delta g_0|^2 [\theta(\varepsilon - \Delta/2) \\ & - \theta(\varepsilon - \Delta/2 - \Omega)]. \end{aligned} \quad (21)$$

Here, the parameter $B(\omega)$ holds information on the phonon properties, such as their density of states and the strength of their coupling to the electrons. $\theta(x)$ is the Heaviside step

function, and

$$\mathcal{L}_{i,j}(\varepsilon, \omega) = \frac{1}{\beta_R \hbar} \begin{pmatrix} e^2 & e(\varepsilon - \omega) & e\omega \\ e\beta_R(\varepsilon - \omega) & (\varepsilon - \omega)^2 & (\varepsilon - \omega)\omega \\ e\beta_R\omega & \omega(\varepsilon - \omega) & \omega^2 \end{pmatrix}. \quad (22)$$

For clarity of the derivation, we fix the origin of energy to the chemical potential, i.e., $\mu_R = 0$. Notice that the density of states in the leads is energy dependent: $\Gamma_L^\varepsilon \propto \theta(-\varepsilon - \Delta/2)$ and $\Gamma_R^\varepsilon \propto \theta(\varepsilon - \Delta/2)$. As a result, the product of four Green's functions in \mathcal{I}_d must describe an electron injected from the left lead at an energy outside the molecule's conduction band, i.e., $\varepsilon - \omega < -\Delta/2$. After absorbing a phonon, the electron, now with energy ε , may enter the conduction band and pass into the right lead. Using the explicit density of states of the leads yields

$$L_{i,j} = \int \frac{d\varepsilon d\omega}{(2\pi)^2} B(\omega) \frac{\partial N_\omega^R}{\partial \omega} \theta(\omega - \Delta) P_{i,j}(\varepsilon, \omega), \quad (23a)$$

$$P_{i,j}(\varepsilon, \omega) = \mathcal{L}_{i,j}(\varepsilon, \omega) [f_R^\varepsilon - f_R^{\varepsilon-\omega}] |g_0|^2 |\delta g_0|^2 [\theta(\varepsilon - \Delta/2) - \theta(\varepsilon - \min\{\omega - \Delta/2, \Delta/2 + \omega\})]. \quad (23b)$$

The expressions for the transport coefficients embody the limitation that phonon absorption is necessary to move between the leads and that only a restricted window of energy can participate in transport per value of ω . Performing the integration over the electronic degree of freedom (ε) is straightforward at low temperatures.

We focus here on the performance of a heat engine operating under the regime of $T_L = T_R$, and $T_{ph} > T_R$. Thus, the second column of the conductivity matrix L [Eq. (6)] is irrelevant. The efficiency of the three-terminal heat engine is the ratio between the generated electric power and the heat current going out of the phonon bath, $\eta = -J_L^e(\Delta\mu/e)/J_{ph}^{th}$. Consequently, the relevant transport coefficients are

$$\begin{pmatrix} J_L \\ J_{ph}^{th} \end{pmatrix} = \tilde{L} \begin{pmatrix} \Delta\mu/e \\ -\Delta\beta_{ph} \end{pmatrix}, \quad (24a)$$

$$\tilde{L} = \begin{pmatrix} G & \alpha_{ph} \\ \beta_R \Pi_{ph} & \kappa_{ph} \end{pmatrix}. \quad (24b)$$

The maximum efficiency, η_{max} , which is given by Eq. (1), is a monotonic function of the figure of merit, $ZT = \alpha_{ph} \Pi_{ph} / GK$ [31,33]. Importantly, the thermal conductivity entering the figure of merit, which is defined in the absence of electric current, is a function of all transport coefficients, $K = \kappa_{ph} - \alpha_{ph} \Pi_{ph} / G$.

To analyze the maximal efficiency and the maximal power for our model, we perform the integral over ε in Eq. (21). As a result, the reduced conductivity matrix takes a simple form,

$$\tilde{L} = G_\Omega \begin{pmatrix} \langle 1 \rangle_\Omega & \langle \omega/e \rangle_\Omega \\ \beta_R \langle \omega/e \rangle_\Omega & \langle \omega^2/e^2 \rangle_\Omega \end{pmatrix}, \quad (25)$$

where the average stands for

$$\langle A(\omega) \rangle_\Omega = \frac{e^2 |g_0|^2 |\delta g_0|^2}{4\pi^2 \beta_R \hbar G_\Omega} \int_\Delta^\infty d\omega A(\omega) B(\omega) \times \min\{\omega - \Delta, \Omega\} \left(-\frac{\partial N_\omega^R}{\partial \omega} \right), \quad (26a)$$

$$G_\Omega = \frac{e^2 |g_0|^2 |\delta g_0|^2}{4\pi^2 \beta_R \hbar} \int_\Delta^\infty d\omega B(\omega) \min\{\omega - \Delta, \Omega\} \times \left(-\frac{\partial N_\omega^R}{\partial \omega} \right). \quad (26b)$$

The equivalent expressions for the complete 3×3 conductivity matrix are given in Appendix B. Following the above derivation, the figure of merit,

$$ZT = [\langle \omega^2 \rangle_\Omega / \langle \omega \rangle_\Omega^2 - 1]^{-1}, \quad (27)$$

acquires the same form as in the work of JEWI [38]. The novelty of their result is in coupling the efficiency to the phonon density of states instead of the electronic one. Mahan and Sofo's "best" thermoelectric [26] was based on narrowing the electronic density of states toward zero. By contrast, JEWI showed that the efficiency can be enhanced by narrowing the phonon band, especially when elastic transport is suppressed. The advantage of our device is that the finite electronic spectrum acts as an energy filter, reducing the weight given to higher frequencies, i.e., effectively narrowing the phonon bandwidth. Consequently, our proposal has the potential to implement thermoelectric devices with high figure of merit.

To demonstrate the advantage of our heat engine relative to that of JEWI, we turn now to analyze ZT as a function of the electronic bandwidth Ω . We offer an intermediate solution between JEWI and Mahan and Sofo—limiting the effective phonon bandwidth *through the electronic spectrum*. Below we refer to the JEWI proposal as one that has unlimited electronic bandwidth, while ours will vary. The figure of merit is inversely proportional to $\zeta_\Omega - 1$, where $\zeta_\Omega = \langle \omega^2 \rangle_\Omega / \langle \omega \rangle_\Omega^2$. Probability theory guarantees that ZT is always positive. Moreover, ZT grows as ζ_Ω becomes closer to unity from above. The efficiencies of the two devices, ours and JEWI's, coincide in the limit $\Omega \rightarrow \infty$. Therefore, we start by expanding ζ_Ω at large Ω ,

$$\zeta_\Omega \approx \zeta_\infty \left[1 - \frac{e^{-\beta(\Delta+\Omega)} (\Delta + \Omega)^{\gamma+2}}{4\pi^2 G_\infty \beta^2 \langle \omega^2 \rangle_\infty} \right]. \quad (28)$$

For the purpose of illustration, we assumed here that $B(\omega) \sim \omega^\gamma$. As expected, we find that ζ_Ω becomes smaller with decreasing Ω . Thus, we established that our device exhibits an improved maximal efficiency once the bandwidth is reduced. To complete the analysis, we also expand ζ_Ω in the limit of vanishing Ω ,

$$\zeta_\Omega = \zeta_0 \left[1 - \frac{\beta \Omega}{2} \frac{2}{(\beta \Delta)^2} \right]. \quad (29)$$

Interestingly, this result indicates that the maximal efficiency grows with electron bandwidth near $\Omega = 0$. Hence, it must have a maximum at an intermediate value of Ω . In Fig. 3 we demonstrate the full dependence of the figure of merit (and

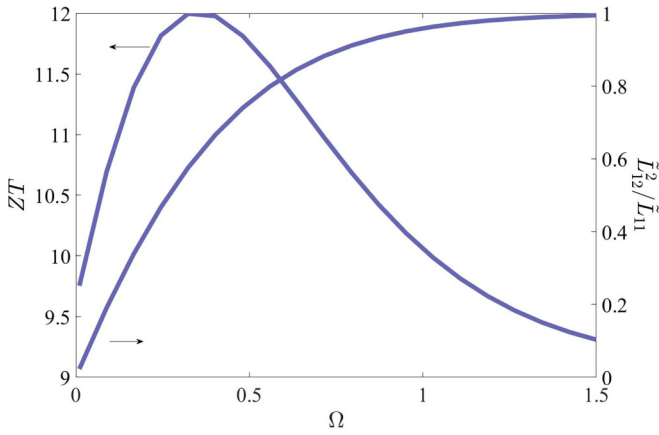


FIG. 3. The figure of merit, ZT , and power factor (normalized by its value at $\Omega \rightarrow \infty$) for our model as function of the bandwidth Ω . The power factor is a monotonic function of the bandwidth, as it is mainly determined by the mean $\langle \omega \rangle_{\Omega}$. The figure of merit, on the other hand, displays the expected maximum. Near the maximum of the figure of merit, the power factor loses only about 30% of its maximum value, improving the engine's efficiency without significant power loss. Parameters chosen are $\beta = 2.5$, $\Delta = 1$ in arbitrary units, and $\gamma = 1$.

hence the maximal efficiency) on Ω for $\gamma = 1$. Since thermoelectric conversion ($\langle \omega \rangle$) contributes to the figure of merit, while thermal conductance ($\langle \omega^2 \rangle$) hinders it, their competition as Ω varies results in the appearance of a maximum, clearly seen in the plot. We refer the reader to Appendix B for a detailed derivation of ζ_{Ω} in the various limits.

The maximal efficiency is not always sufficient to characterize thermoelectric devices. The maximum power P_{\max} and the efficiency at maximum power $\eta(P_{\max}) = \frac{\eta_c}{2} \frac{ZT}{2+ZT}$ are often equally or even more important. The material dependence of the maximum power $P_{\max} = \tilde{L}_{12}^2 / \tilde{L}_{11} (\Delta \beta_{\text{ph}})^2 / 4$ is contained in the so-called power factor $\tilde{L}_{12}^2 / \tilde{L}_{11}$. The dependence of $\eta(P_{\max})$ on ZT is similar to η_{\max} , and therefore benefits from our architecture as well. By contrast, the power factor, here taking the form $G_{\Omega} \langle \omega \rangle_{\Omega}^2$, grows monotonically with Ω , approaching its highest value for $\Omega \rightarrow \infty$. Thus, it is clear that reducing the electronic bandwidth Ω lowers the power production of our heat engine. However, a more quantitative analysis of the power factor allows more delicate optimization of the engine. In particular, the rate at which it changes with decreasing Ω determines whether operating at maximum efficiency must come at the cost of low power. Applying the same assumptions we used in our calculation of ZT , we find the power factor and plot them together in Fig. 3. Indeed, the power factor remains significant near the maximum. In addition, we analyze the limits of Ω going to zero and to infinity:

$$G_{\Omega} \langle \omega \rangle_{\Omega}^2 \approx \begin{cases} G_{\infty} \langle \omega \rangle_{\infty}^2 \left[1 - \frac{e^{-\beta(\Delta+\Omega)} \Omega^{\gamma+1}}{2\pi \beta^2 \langle \omega \rangle_{\infty} \beta G_{\infty}} \right], & \Omega \rightarrow \infty \\ \Omega \frac{e^{-\beta \Delta} \Delta^{\gamma+2}}{\beta (2\pi)^2} \left[1 + \frac{\gamma+2}{\beta \Delta} \right], & \Omega \rightarrow 0. \end{cases} \quad (30)$$

We find that the strongest change in the power factor occurs at $\Omega \lesssim \Delta$. Consequently, our device is optimal in systems where the figure of merit has a maximum at $\Omega > T$.

To conclude this section, our simple analysis reveals that a limited electronic bandwidth is beneficial for thermoelectric conversion in systems where elastic transport is suppressed. However, the power factor in such engines tends to be smaller than the one obtained for an unrestricted electronic band. Nevertheless, we obtained that the reduction in the power factor can still be moderate near the maximum of the figure of merit (see Fig. 3). Therefore, we can benefit from the improved efficiency with only a small loss in the generated power. In the next section, we show that our thermoelectric device can be implemented by a chiral molecule exhibiting CISS bridging two magnetic leads.

VI. MODEL FOR CISS-BASED THERMOELECTRIC DEVICE

The CISS effect has been observed in many different chiral structures, ranging from short organic molecules to super-helical polymer microfibers [56], and even two-dimensional chiral hybrid organic-inorganic perovskites [57–59]. To model CISS, we need a simple model that captures universal features such as the molecule's helical structure, and realizes spin-dependent transport. In a previous work [46], we showed that a helix-shaped atomic chain gives rise to a strong spin-dependent transport in the presence of SOC and electron-phonon interactions. Importantly, the low-energy degrees of freedom of the chain must include at least two orbital modes with the same total angular momentum but different $|\ell|$. To connect the toy model analyzed in the previous section and a more realistic model of systems supporting CISS, we follow the model of Ref. [46] and replace the first term in Eq. (9) by

$$\mathcal{H}_{\text{mol}}^{\text{el}} = \sum_{n,\ell,s} \tilde{t} [c_{n,\ell,s}^{\dagger} c_{n+1,\ell,s} + c_{n+1,\ell,s}^{\dagger} c_{n,\ell,s}] + \Delta_{\text{soc}} \times \sum_{n,\ell,s,s'} \ell \left[\chi \sin \frac{2\pi n}{\tilde{R}} \sigma_x - \cos \frac{2\pi n}{\tilde{R}} \sigma_y - \frac{b}{2\pi R} \sigma_z \right]. \quad (31)$$

Here the quantization axis of the electron spin s is along the center of the helix, which we denote as the z direction, and σ_i are the Pauli matrices. The first term describes the kinetic energy associated with hopping between neighboring atoms along the helix. The second term is the atomic SOC that on the helical lattice simply favors spin alignment of a state with $\ell \neq 0$ in the direction of the chemical bonds. The parameters b and R are the pitch and radius of the helix, $\tilde{R} = \sqrt{(2\pi R)^2 + b^2}$, and $\chi = \pm$ denotes the handedness of the atomic helix. In this model, only $\ell \neq 0$ bands, which are typically responsible for charge transfer via organic molecules, experience SOC. To simplify our calculation, we focus here on states with $\ell = \pm 1$, i.e., on transport through p_x and p_y orbitals. In addition, we neglect the last term of the SOC in Eq. (31), since it has a limited influence on the strength of the CISS effect. The above Hamiltonian is the low-energy limit of the models used in Refs. [47,60–62] for demonstrating spin-dependent transport through chiral molecules.

In the absence of electron-phonon interactions, the energy spectrum corresponding to the Hamiltonian in Eq. (31) has a narrow partial gap of width $\sim 2\Delta_{\text{soc}}$. The remaining states within this partial gap, which results from the SOC term,

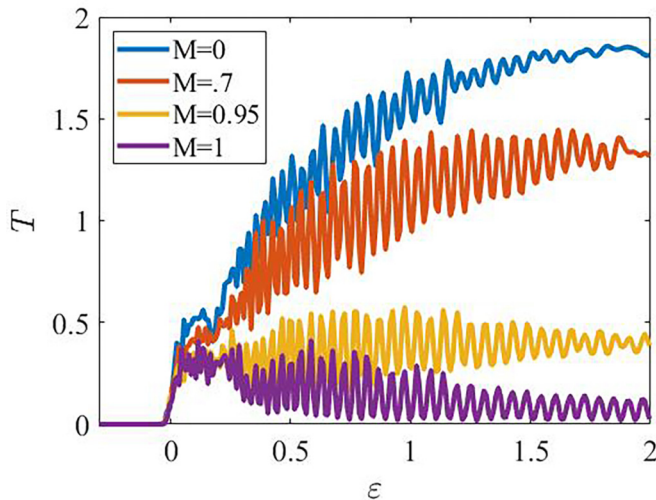


FIG. 4. Transmission through the molecule as a function of energy for various magnetization strengths of the leads, M . Transmission outside the partial gap is largely suppressed as the leads become more spin polarized in opposite directions. The transmission remains effective only at energies where the possibility of a spin flip is available, i.e., within the partial gap of width $\sim 2\Delta_{\text{SOC}}$ near the bottom of the band. Notice that we add a small disorder potential to smooth out resonances in the transmission, a result of the molecule being finite.

support spin-dependent transport. An electron carrying a given spin has unequal probabilities of passing from left to right and from right to left. Equivalently, the spin of an electron passing through the system at the energies of the partial gap gets polarized according to the direction of propagation. In Ref. [46], we showed that in the strongly interacting polaron limit, significant spin-dependent transport is obtained even when the chemical potentials of both leads are far below the bottom of the molecule's conduction band. Charge transport at energies within the band gap is supported solely by phonon absorption. With the additional energy from an absorbed phonon, the polaron energy can reach the band and propagate through the molecule. In this case, spin-dependent transport is observed if the polaron's final energy ε coincides with the partial energy gap $\varepsilon_0 - \Delta_{\text{SOC}} < \varepsilon < \varepsilon_0 + \Delta_{\text{SOC}}$, with ε_0 being the middle of the gap.

To implement the physics of the previous toy model, the electrodes should be strongly magnetized in opposite directions. As before, the left lead has states only below the molecule spectrum, and the right lead has states only at energies overlapping the molecule spectrum and above. The chemical potentials in both leads are fixed to the band gap. In Fig. 4 we plot the noninteracting transmission through the molecule as the magnetization in the leads $M \equiv M^L = (\Gamma_{\uparrow}^L - \Gamma_{\downarrow}^L)/\Gamma_{\uparrow}^L = -M^R$ becomes stronger. Electron transmission through the molecule is strongly suppressed outside the partial energy gap (located near the bottom of the band). Since the chemical potentials of the leads are far below the band, the conductivity in the absence of interactions is negligible. Significant transport occurs only in the presence of interactions. An electron may enter the molecule through a decaying polaron state at energies within the band gap, and encounter a

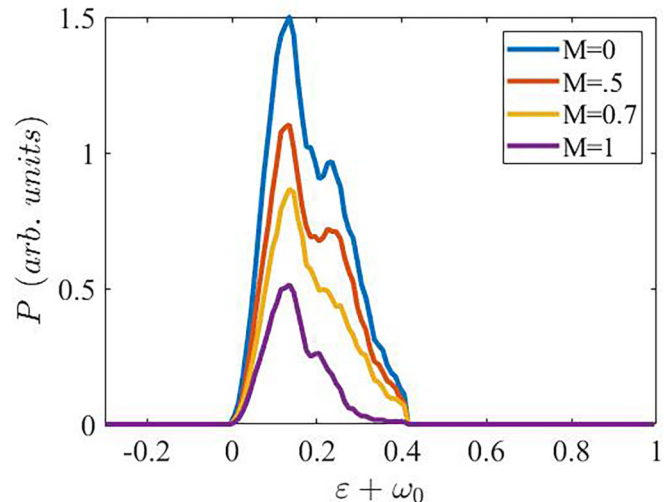


FIG. 5. The integrand of the electric conductance $P(\varepsilon, \omega)$ in the presence of interactions as a function of energy ε for various strengths of the leads magnetization. For strongly spin-polarized leads, the main contribution to the conductance that can reach the partial gap by absorbing a phonon, $\varepsilon_0 - \Delta_{\text{SOC}} - \omega \lesssim \varepsilon \lesssim \varepsilon_0 + \Delta_{\text{SOC}} - \omega$.

phonon fluctuation. Then, absorption of a phonon may take the polaron into energies in the window $\varepsilon_0 - \Delta_{\text{SOC}} < \varepsilon < \varepsilon_0 + \Delta_{\text{SOC}}$, where a spin flip allows it to pass and relax into the opposite lead. Importantly, this is the main mechanism for conduction through the system. As a consequence, our system implements the toy model by having a narrow effective conduction band of width $2\Delta_{\text{SOC}}$.

We demonstrate these properties of the system by calculating the main contribution to the conductance from Eqs. (18) and (19). In Fig. 5 we show the integrand $P_{1,1}(\varepsilon, \omega_0)$ in Eq. (23b) as a function of energy for different magnetization strengths of the leads and a single optical phonon frequency ω_0 . As expected, increasing the imbalance between spins in the leads strongly reduces $P_{1,1}(\varepsilon, \omega_0)$ at energies above the partial gap, while contributions from $\varepsilon_0 - \Delta_{\text{SOC}} < \varepsilon + \omega_0 < \varepsilon_0 + \Delta_{\text{SOC}}$ remain relatively large. The only difference between the contribution to the currents from the toy model and the chiral molecule is that the polaron Green's function is not constant for the latter. We expect such a modification to have only a small qualitative effect. The purpose of this work is to qualitatively show the potential benefits of using chiral molecules for thermoelectric applications. We leave more accurate calculations based on specific microscopic models of the molecules for future work. Nevertheless, we have provided a general framework for characterizing CISS-based thermoelectric devices that requires only derivation of the noninteracting properties of the molecule.

We focus in this work on the effect of optical phonons on thermoelectric transport through chiral molecules since the majority of vibrations in these systems are of localized charges. Furthermore, Peralta *et al.* have shown that optical phonons are more dominantly coupled to electron transport in molecules [63].

We note that our focus here is the analysis of transport in the case of strongly polarized magnetic leads. When the

magnetization is not so strong, the chiral molecules also exhibit an asymmetry in thermopower, whose advantages were first explored in Ref. [31]. Such asymmetry is theorized to occur also in Aharonov-Bohm interferometers connected to several reservoirs [32,35], chiral quantum Hall edge states [64], and more generally in systems where interactions or dephasing affect transport properties [65].

VII. CONCLUSIONS

We have shown that chiral molecules mounted between two opposite magnets can implement efficient thermoelectric machines due to their nontrivial transport properties. In such systems, absorption and emission of phonons by incoming electrons becomes correlated with the possibility to flip spin, thus generating a thin window for conduction on the order of the SOC. Specifically, the figure of merit can increase by 30% compared to similar systems studied in the past, without significant loss of power.

Our results are not limited to single-molecule engines, but can also be applied to materials containing chiral components,

e.g., chiral hybrid organic-inorganic perovskites [57,59]. The multitude of alternatives presented here make chiral thermoelectric engines a highly realizable solution to the removal of heat from microprocessors, one of the major limiting factors of further miniaturization. In addition, as a heat engine, our proposal can make use of waste heat to efficiently generate electricity. Finally, magnetoresistance measurements involving chiral structures are usually performed at ambient conditions, with magnet strengths ranging on the order of 1 T. While the efficiency of the thermoelectric engine grows with the lead magnetic moment, as shown in Fig. 5, it is already significant at moderate magnetization. In fact, using magnetic leads of intermediate magnetization level is beneficial for achieving a reasonable efficiency without compromising much on the power production.

ACKNOWLEDGMENT

This work was supported by the Minerva foundation with funding from the Federal German Ministry for Education and Research.

APPENDIX A: EXPRESSIONS FOR TRANSPORT COEFFICIENTS

The expressions for the electric and heat currents in the left lead are written in Eq. (17). Similarly, we can find the contributions to the currents flowing into the right lead by substituting $R \leftrightarrow L$. The transport coefficients can be extracted from the currents in both leads as well as the conservation laws in Eq. (3). For this purpose, we consider the regime of linear response; i.e., we expand the current up to the first order in $\Delta\beta_L$, $\Delta\beta_{\text{ph}}$, and $\Delta\mu$. The corresponding transport coefficients are

$$G = -\frac{e^2}{\hbar} \int \frac{d\varepsilon}{2\pi} \mathcal{I}_a \frac{df}{dx} \beta_R + \frac{e^2}{2\hbar} \int \frac{d\varepsilon d\omega}{(2\pi)^2} [\mathcal{I}_b + \mathcal{I}_c + 2i\mathcal{I}_d] [f^\varepsilon - f^{\varepsilon-\omega}] \frac{dN}{dx} \beta_R, \quad (\text{A1a})$$

$$\alpha_1 = -\frac{e}{\hbar} \int \frac{d\varepsilon}{2\pi} \mathcal{I}_a (\varepsilon - \mu) \frac{df}{dx} + \frac{e}{2\hbar} \int \frac{d\varepsilon d\omega}{(2\pi)^2} [f^\varepsilon - f^{\varepsilon-\omega}] \frac{dN}{dx} \times \{(\varepsilon - \mu)\mathcal{I}_b + (\varepsilon - \omega - \mu)(\mathcal{I}_c + 2i\mathcal{I}_d) - 2i\omega\mathcal{I}_e\}, \quad (\text{A1b})$$

$$\alpha_{\text{ph}} = \frac{e}{\hbar} \int \frac{d\varepsilon d\omega}{(2\pi)^2} [f^\varepsilon - f^{\varepsilon-\omega}] \frac{dN}{dx} \{i\omega(\mathcal{I}_d + \mathcal{I}_e)\}, \quad (\text{A1c})$$

$$\Pi_1 = -\frac{e}{\hbar} \int \frac{d\varepsilon}{2\pi} \mathcal{I}_a (\varepsilon - \mu) \frac{df}{dx} + \frac{e}{2\hbar} \int \frac{d\varepsilon d\omega}{(2\pi)^2} [f^\varepsilon - f^{\varepsilon-\omega}] \frac{dN}{dx} \{(\varepsilon - \mu)\mathcal{I}_b + (\varepsilon - \omega - \mu)(\mathcal{I}_c + 2i\mathcal{I}_d)\}, \quad (\text{A1d})$$

$$\kappa_{\text{LR}} = -\frac{1}{\hbar} \int \frac{d\varepsilon}{2\pi} \mathcal{I}_a (\varepsilon - \mu)^2 \frac{df}{dx} + \frac{1}{2\hbar} \int \frac{d\varepsilon d\omega}{(2\pi)^2} [f^\varepsilon - f^{\varepsilon-\omega}] \frac{dN}{dx} \times \{(\varepsilon - \mu)^2\mathcal{I}_b + (\varepsilon - \omega - \mu)^2(\mathcal{I}_c + 2i\mathcal{I}_d) - 2i(\varepsilon - \omega - \mu)\omega\mathcal{I}_e\}, \quad (\text{A1e})$$

$$\kappa_{\text{L,ph}} = \frac{1}{\hbar} \int \frac{d\varepsilon d\omega}{(2\pi)^2} [f^\varepsilon - f^{\varepsilon-\omega}] \frac{dN}{dx} \{(\varepsilon - \omega - \mu)\omega(i\mathcal{I}_d + i\mathcal{I}_e)\}, \quad (\text{A1f})$$

$$\Pi_{\text{ph}} = -\frac{e}{2\hbar} \int \frac{d\varepsilon d\omega}{(2\pi)^2} [f^\varepsilon - f^{\varepsilon-\omega}] \frac{dN}{dx} \{\varepsilon(\mathcal{I}_b - \bar{\mathcal{I}}_c - 2i\bar{\mathcal{I}}_d) + (\varepsilon - \omega)(\mathcal{I}_c - \bar{\mathcal{I}}_b + 2i\mathcal{I}_d)\}, \quad (\text{A1g})$$

$$\kappa_{\text{ph,L}} = \frac{1}{2\hbar} \int \frac{d\varepsilon d\omega}{(2\pi)^2} [f^\varepsilon - f^{\varepsilon-\omega}] \frac{dN}{dx} \times \{-\varepsilon(\varepsilon - \mu)(\mathcal{I}_b - \bar{\mathcal{I}}_c) + (\varepsilon - \omega)(\varepsilon - \omega - \mu)(-\mathcal{I}_c - 2i\mathcal{I}_d + \bar{\mathcal{I}}_b) + 2i(\varepsilon - \omega)\omega\mathcal{I}_e + \varepsilon(\varepsilon - \omega - \mu)2i\bar{\mathcal{I}}_d\}, \quad (\text{A1h})$$

$$\kappa_{\text{ph}} = \frac{1}{\hbar} \int \frac{d\varepsilon d\omega}{(2\pi)^2} [f^\varepsilon - f^{\varepsilon-\omega}] \frac{dN}{dx} \{-(\varepsilon - \omega)\omega(i\mathcal{I}_d + i\mathcal{I}_e) + \varepsilon\omega(i\bar{\mathcal{I}}_d + i\bar{\mathcal{I}}_e)\}. \quad (\text{A1i})$$

Above and in the main part of the text, the currents and the corresponding transport coefficients are written using a diagrammatic representation. Here, we provide explicit expressions for the various diagrams entering Eq. (17):

$$\mathcal{I}_a = [g^R \cdot \Gamma_R \cdot g^A \cdot \Gamma_L]_{n,s;n,s}^\varepsilon, \quad (\text{A2a})$$

$$\mathcal{I}_b = [g^R \cdot \Gamma_R \cdot g^A \cdot \Gamma_L \cdot g^R - g^A \cdot \Gamma_L \cdot g^R \cdot \Gamma_R \cdot g^A]_{n,s;n',s'}^\varepsilon [D^R - D^A]_{n',p';p,n}^\omega \cdot [g^R \cdot \Gamma_L \cdot g^A]_{p',s';p,s}^{\varepsilon-\omega}, \quad (\text{A2b})$$

$$\mathcal{I}_c = [g^R \cdot \Gamma_R \cdot g^A \cdot \Gamma_L \cdot g^R - g^A \cdot \Gamma_L \cdot g^R \cdot \Gamma_R \cdot g^A]_{n,s;n',s'}^{\varepsilon-\omega} [D^R - D^A]_{n',p';p,n}^{\omega} \cdot [g^R \cdot \Gamma_R \cdot g^A]_{p',s';p,s}^{\varepsilon}, \quad (\text{A2c})$$

$$\mathcal{I}_d = [g^A \cdot \Gamma_L \cdot g^R]_{n,s;n',s'}^{\varepsilon-\omega} [D^R - D^A]_{n',p';p,n}^{\omega} \cdot [g^R \cdot \Gamma_R \cdot g^A]_{p',s';p,s}^{\varepsilon}, \quad (\text{A2d})$$

$$\mathcal{I}_e = [g^A \cdot \Gamma_L \cdot g^R]_{n,s;n',s'}^{\varepsilon-\omega} [D^R - D^A]_{n',p';p,n}^{\omega} \cdot [g^R \cdot \Gamma_L \cdot g^A]_{p',s';p,s}^{\varepsilon}. \quad (\text{A2e})$$

We note that we neglect real corrections to the self-energy since their contribution is negligible for transport below the conduction bands. Similarly, we find the contributions to the currents flowing into the right lead by substituting $R \leftrightarrow L$ and performing the transformations $\varepsilon \rightarrow \varepsilon + \omega$ as well as $\omega \rightarrow -\omega$ in Eq. (17) and in all of the above diagrams. We denote the corresponding diagrams by $\tilde{\mathcal{I}}_\alpha$.

APPENDIX B: CALCULATION OF THE FULL CONDUCTIVITY MATRIX FOR THE TOY MODEL

In the main text, we write the reduced 2×2 conductivity matrix \tilde{L} that determines the properties of the three-terminal thermoelectric devices. For completeness, we give here the expression for the full 3×3 conductivity matrix obtained after performing the integral over ε in Eq. (21):

$$L = G_\Omega \begin{pmatrix} \langle 1 \rangle_\Omega & \langle f_1(\omega)/e \rangle_\Omega & \langle \omega/e \rangle_\Omega \\ \beta_R \langle f_1(\omega)/e \rangle_\Omega & \langle f_2(\omega)/e^2 \rangle_\Omega & \langle f_3(\omega)/e^2 \rangle_\Omega \\ \beta_R \langle \omega/e \rangle_\Omega & \langle f_3(\omega)/e^2 \rangle_\Omega & \langle \omega^2/e^2 \rangle_\Omega \end{pmatrix}. \quad (\text{B1})$$

The functions f_i are

$$f_1(\omega) = \begin{cases} -\omega/2, & \Delta < \omega < \Omega + \Delta \\ -\omega + (\Omega + \Delta)/2, & \Omega + \Delta < \omega, \end{cases} \quad (\text{B2})$$

$$f_2(\omega) = \begin{cases} (\omega^2 - \omega\Delta/2 + (\Delta/2)^2)/3, & \Delta < \omega < \Omega + \Delta \\ (3\omega^2 - 3\omega(\Omega + \Delta) + \Omega^2 + 3(\Delta/2)^2 + 3\Omega\Delta/2)/3, & \Omega + \Delta < \omega, \end{cases} \quad (\text{B3})$$

$$f_3(\omega) = \begin{cases} -\omega^2/2, & \Delta < \omega < \Omega + \Delta \\ -\omega^2 + \omega(\Omega + \Delta)/2, & \Omega + \Delta < \omega. \end{cases} \quad (\text{B4})$$

Next, we derive the asymptotic expressions for the various transport coefficients in the limits $\Omega \rightarrow \infty$ and $\Omega \rightarrow 0$. For this purpose, it is sufficient to examine the generic form of the integral

$$M_n(\Omega) = \frac{1}{2\pi\beta} \int_{-\infty}^{\infty} \frac{d\omega}{2\pi} \omega^n \theta(\omega - \Delta) \min\{\omega - \Delta, \Omega\} \left(-\frac{dN}{d\omega} \right) B(\omega), \quad (\text{B5})$$

where the power n is different for each component of the conductivity matrix. For example, $n = 0$ and $n = 2$ for the electric and thermal conductance, respectively. At large Ω , the above integral can be written as

$$M_n(\Omega) = G_\infty \langle \omega^n \rangle_\infty + \frac{1}{2\pi} \int_{\Delta+\Omega}^{\infty} \frac{d\omega}{2\pi\beta} \omega^n (\Delta + \Omega - \omega) \left(-\frac{dN}{d\omega} \right) B(\omega). \quad (\text{B6})$$

In the limit of low temperatures, $\beta\Delta \gtrsim 1$, the Bose function may be approximated to be $N(\omega) \sim e^{-\beta\omega}$. Then, assuming $B(\omega) \sim \omega^\gamma$ and performing the integral by parts, we find

$$\frac{1}{2\pi\beta^{n+\gamma+2}} \int_{\beta(\Delta+\Omega)}^{\infty} \frac{d(\beta\omega)}{2\pi} (\beta\omega)^{n+\gamma} (\beta(\Delta + \Omega) - \beta\omega) e^{-\beta\omega} \approx -\frac{e^{-\beta(\Delta+\Omega)} (\Delta + \Omega)^{n+\gamma}}{(2\pi)^2 \beta^2}. \quad (\text{B7})$$

Similarly, we can find the $M_n(\Omega)$ in the limit $\Omega \rightarrow 0$,

$$M_n(\Omega) \approx \Omega \int_{\beta\Delta}^{\infty} \frac{d(\beta\omega)}{4\pi^2 \beta^{n+\gamma+2}} (\beta\omega)^{n+\gamma} e^{-\beta\omega} = \Omega \frac{\Gamma(n + \gamma + 1, \beta\Delta)}{4\pi^2 \beta^{n+\gamma+2}}, \quad (\text{B8})$$

where $\Gamma(a, z)$ is the incomplete gamma function.

- [1] K. Ray, S. P. Ananthavel, D. H. Waldeck, and R. Naaman, Asymmetric scattering of polarized electrons by organized organic films of chiral molecules, *Science* **283**, 814 (1999).
 [2] B. Göhler, V. Hamelbeck, T. Z. Markus, M. Kettner, G. F. Hanne, Z. Vager, R. Naaman, and H. Zacharias, Spin selectivity in electron transmission through self-assembled monolayers of double-stranded DNA, *Science* **331**, 894 (2011).

- [3] M. Kettner, B. Goehler, H. Zacharias, D. Mishra, V. Kiran, R. Naaman, C. Fontanesi, D. H. Waldeck, S. Sek, J. Pawowski, and J. Juhaniewicz, Spin filtering in electron transport through chiral oligopeptides, *J. Phys. Chem. C* **119**, 14542 (2015).
 [4] Z. Xie, T. Z. Markus, S. R. Cohen, Z. Vager, R. Gutierrez, and R. Naaman, Spin specific electron conduction through DNA oligomers, *Nano Lett.* **11**, 4652 (2011).

- [5] V. Kiran, S. Cohen, and R. Naaman, Structure dependent spin selectivity in electron transport through oligopeptides, *J. Chem. Phys.* **146**, 092302 (2017).
- [6] K. Banerjee-Ghosh, A. Capua, O. Ben Dor, F. Tassinari, K. Banerjee-Ghosh, L. Kronik, S. Yochelis, S. S. P. Parkin, S.-H. Yang, E. Capua, S. Sarkar, Y. Paltiel, and L. T. Baczewski, Separation of enantiomers by their enantiospecific interaction with achiral magnetic substrates, *Science* **360**, 1331 (2018).
- [7] S. Alwan and Y. Dubi, Spinterface origin for the chirality-induced spin-selectivity effect, *J. Am. Chem. Soc.* **143**, 14235 (2021).
- [8] A.-M. Guo and Q.-F. Sun, Spin-Selective Transport of Electrons in DNA Double Helix, *Phys. Rev. Lett.* **108**, 218102 (2012).
- [9] A.-M. Guo and Q.-F. Sun, Spin-dependent electron transport in protein-like single-helical molecules, *Proc. Natl. Acad. Sci. USA* **111**, 11658 (2014).
- [10] R. Gutierrez, E. Diaz, R. Naaman, and G. Cuniberti, Spin-selective transport through helical molecular systems, *Phys. Rev. B* **85**, 081404(R) (2012).
- [11] R. Gutierrez, E. Diaz, C. Gaul, T. Brumme, F. Dominguez-Adame, and G. Cuniberti, Modeling spin transport in helical fields: Derivation of an effective low-dimensional Hamiltonian, *J. Phys. Chem. C* **117**, 22276 (2013).
- [12] S. Varela, E. Medina, F. Lopez, and V. Mujica, Inelastic electron scattering from a helical potential: Transverse polarization and the structure factor in the single scattering approximation, *J. Phys.: Condens. Matter* **26**, 015008 (2014).
- [13] E. Medina, F. Lopez, M. A. Ratner, and V. Mujica, Chiral molecular films as electron polarizers and polarization modulators, *Europhys. Lett.* **99**, 17006 (2012).
- [14] A. A. Eremko and V. M. Loktev, Spin sensitive electron transmission through helical potentials, *Phys. Rev. B* **88**, 165409 (2013).
- [15] S. Matityahu, Y. Utsumi, A. Aharony, O. Entin-Wohlman, and C. A. Balseiro, Spin-dependent transport through a chiral molecule in the presence of spin-orbit interaction and nonunitary effects, *Phys. Rev. B* **93**, 075407 (2016).
- [16] O. Entin-Wohlman, A. Aharony, and Y. Utsumi, Comment on "Spin-orbit interaction and spin selectivity for tunneling electron transfer in DNA", *Phys. Rev. B* **103**, 077401 (2021).
- [17] S. P. Mathew, P. C. Mondal, H. Moshe, Y. Mastai, and R. Naaman, Non-magnetic organic/inorganic spin injector at room temperature, *Appl. Phys. Lett.* **105**, 242408 (2014).
- [18] O. Ben Dor, N. Morali, S. Yochelis, L. T. Baczewski, and Y. Paltiel, Local light-induced magnetization using nanodots and chiral molecules, *Nano Lett.* **14**, 6042 (2014).
- [19] O. Ben Dor, S. Yochelis, A. Radko, K. Vankayala, E. Capua, A. Capua, S. H. Yang, L. T. Baczewski, S. S. P. Parkin, R. Naaman, and Y. Paltiel, Magnetization switching in ferromagnets by adsorbed chiral molecules without current or external magnetic field, *Nat. Commun.* **8**, 14567 (2017).
- [20] O. Fenwick and A. Jones, Materials for the energy transition roadmap: Thermoelectric energy conversion materials, Henry Royce Institute, 2020 (unpublished), <https://www.royce.ac.uk/materials-for-the-energy-transition-thermoelectric-energy-conversion/>.
- [21] J. P. Heremans, M. S. Dresselhaus, L. E. Bell, and D. T. Morelli, When thermoelectrics reached the nanoscale, *Nat. Nanotechnol.* **8**, 471 (2013).
- [22] L. E. Bell, Cooling, heating, generating power, and recovering waste heat with thermoelectric systems, *Science* **321**, 1457 (2008).
- [23] B. Hinterleitner, I. Knapp, M. Ponerer, Y. Shi, H. Müller, G. Eguchi, C. Eisenmenger-Sittner, M. Stöger-Pollach, Y. Kakefuda, N. Kawamoto, Q. Guo, T. Baba, T. Mori, S. Ullah, X. Q. Chen, and E. Bauer, Thermoelectric performance of a metastable thin-film Heusler alloy, *Nature (London)* **576**, 85 (2019).
- [24] K. Xia, C. Hu, C. Fu, X. Zhao, and T. Zhu, Half-Heusler thermoelectric materials, *Appl. Phys. Lett.* **118**, 140503 (2021).
- [25] N. Xu, Y. Xu, and J. Zhu, Topological insulators for thermoelectrics, *npj Quantum Mater.* **2**, 51 (2017).
- [26] G. D. Mahan and J. O. Sofo, The best thermoelectric, *Proc. Natl. Acad. Sci. USA* **93**, 7436 (1996).
- [27] T. E. Humphrey and H. Linke, Reversible Thermoelectric Nanomaterials, *Phys. Rev. Lett.* **94**, 096601 (2005).
- [28] G. Haack and F. Giazotto, Efficient and tunable Aharonov-Bohm quantum heat engine, *Phys. Rev. B* **100**, 235442 (2019).
- [29] N. W. Ashcroft and N. D. Mermin, *Solid State Physics* (Saunders College Publishing, New York, 1976).
- [30] H. B. G. Casimir, On Onsager's principle of microscopic reversibility, *Rev. Mod. Phys.* **17**, 343 (1945).
- [31] G. Benenti, K. Saito, and G. Casati, Thermodynamic Bounds on Efficiency for Systems with Broken Time-Reversal Symmetry, *Phys. Rev. Lett.* **106**, 230602 (2011).
- [32] V. Balachandran, G. Benenti, and G. Casati, Efficiency of three-terminal thermoelectric transport under broken time-reversal symmetry, *Phys. Rev. B* **87**, 165419 (2013).
- [33] K. Brandner, K. Saito, and U. Seifert, Strong Bounds on Onsager Coefficients and Efficiency for Three-Terminal Thermoelectric Transport in a Magnetic Field, *Phys. Rev. Lett.* **110**, 070603 (2013).
- [34] K. Brandner and U. Seifert, Multi-terminal thermoelectric transport in a magnetic field: Bounds on Onsager coefficients and efficiency, *New J. Phys.* **15**, 105003 (2013).
- [35] O. Entin-Wohlman and A. Aharony, Three-terminal thermoelectric transport under broken time-reversal symmetry, *Phys. Rev. B* **85**, 085401 (2012).
- [36] K. Yamamoto, O. Entin-Wohlman, A. Aharony, and N. Hatano, Efficiency bounds on thermoelectric transport in magnetic fields: The role of inelastic processes, *Phys. Rev. B* **94**, 121402(R) (2016).
- [37] O. Entin-Wohlman, Y. Imry, and A. Aharony, Three terminal thermoelectric transport through a molecular junction, *Phys. Rev. B* **82**, 115314 (2010).
- [38] J. H. Jiang, O. Entin-Wohlman, and Y. Imry, Three terminal semiconductor junction thermoelectric devices: Improving performance, *New J. Phys.* **15**, 075021 (2013).
- [39] J. H. Jiang, M. Kulkarni, D. Segal, and Y. Imry, Phonon thermoelectric transistors and rectifiers, *Phys. Rev. B* **92**, 045309 (2015).
- [40] X. Yang, C. H. van der Wal, and B. J. van Wees, Spin-dependent electron transmission model for chiral molecules in mesoscopic devices, *Phys. Rev. B* **99**, 024418 (2019).
- [41] J. Fransson, Vibrational origin of exchange splitting and chirality-induced spin selectivity, *Phys. Rev. B* **102**, 235416 (2020).
- [42] G. F. Du, H. H. Fu, and R. Wu, Vibration-enhanced spin-selective transport of electrons in the DNA double helix, *Phys. Rev. B* **102**, 035431 (2020).

- [43] L. Zhang, Y. Hao, W. Qin, S. Xie, and F. Qu, Chiral-induced spin selectivity: A polaron transport model, *Phys. Rev. B* **102**, 214303 (2020).
- [44] E. Díaz, P. Albares, P. G. Estevez, J. M. Cervero, C. Gaul, E. Diez, and F. Domínguez-Adame, Spin dynamics in helical molecules with nonlinear interactions, *New J. Phys.* **20**, 043055 (2018).
- [45] E. Díaz, A. Contreras, J. Hernández, and F. Domínguez-Adame, Effective nonlinear model for electron transport in deformable helical molecules, *Phys. Rev. E* **98**, 052221 (2018).
- [46] D. Klein and K. Michaeli, Giant chirality-induced spin selectivity of polarons, *Phys. Rev. B* **107**, 045404 (2023).
- [47] K. Michaeli and R. Naaman, Origin of spin dependent tunneling through chiral molecules, *J. Phys. Chem. C* **123**, 17043 (2019).
- [48] L. Onsager, Reciprocal relations in irreversible processes, *Phys. Rev.* **37**, 405 (1931).
- [49] A. C. Domenicali, Irreversible thermodynamics of thermoelectricity, *Rev. Mod. Phys.* **26**, 237 (1954).
- [50] H. Fröhlich, Electrons in lattice fields, *Adv. Phys.* **3**, 325 (1954).
- [51] T. Holstein, Studies of polaron motion: Part II. The “small” polaron, *Ann. Phys.* **8**, 343 (1959).
- [52] G. D. Mahan, *Many-Particle Physics* (Springer US, Boston, 2000).
- [53] Y. Meir and N. S. Wingreen, Landauer Formula for the Current through an Interacting Electron Region, *Phys. Rev. Lett.* **68**, 2512 (1992).
- [54] J. Rammer and H. Smith, Quantum field-theoretical methods in transport theory of metals, *Rev. Mod. Phys.* **58**, 323 (1986).
- [55] J. P. Ellis, TikZ-Feynman: Feynman diagrams with TikZ, *Comput. Phys. Commun.* **210**, 103 (2017).
- [56] L. Jia, C. Wang, Y. Zhang, L. Yang, and Y. Yan, Efficient spin selectivity in self-assembled superhelical conducting polymer microfibers, *ACS Nano* **14**, 6607 (2020).
- [57] H. Lu, J. Wang, C. Xiao, X. Pan, X. Chen, R. Brunecky, J. J. Berry, K. Zhu, M. C. Beard, and Z. V. Vardeny, Spin-dependent charge transport through 2D chiral hybrid lead-iodide perovskites, *Sci. Adv.* **5**, eaay0571 (2019).
- [58] Z. Huang, B. P. Bloom, X. Ni, Z. N. Georgieva, M. Marciesky, E. Vetter, F. Liu, D. H. Waldeck, and D. Sun, Magneto-optical detection of photoinduced magnetism via chirality-induced spin selectivity in 2D chiral hybrid organic-inorganic perovskites, *ACS Nano* **14**, 10370 (2020).
- [59] H. Lu, C. Xiao, R. Song, T. Li, A. E. Maughan, A. Levin, R. Brunecky, J. J. Berry, D. B. Mitzi, V. Blum, and M. C. Beard, Highly distorted chiral two-dimensional tin iodide perovskites for spin polarized charge transport, *J. Am. Chem. Soc.* **142**, 13030 (2020).
- [60] S. Dalum and P. Hedegard, Theory of chiral induced spin selectivity, *Nano Lett.* **19**, 5253 (2019).
- [61] Y. Utsumi, O. Entin-Wohlman, and A. Aharony, Spin selectivity through time-reversal symmetric helical junctions, *Phys. Rev. B* **102**, 035445 (2020).
- [62] M. Geyer, R. Gutierrez, and G. Cuniberti, Effective Hamiltonian model for helically constrained quantum systems within adiabatic perturbation theory: Application to the chirality-induced spin selectivity (CISS) effect, *J. Chem. Phys.* **152**, 214105 (2020).
- [63] M. Peralta, S. Feijoo, S. Varela, V. Mujica, and E. Medina, Coherence preservation and electron-phonon interaction in electron transfer in DNA, *J. Chem. Phys.* **153**, 165102 (2020).
- [64] R. Sanchez, B. Sothmann, and A. N. Jordan, Chiral Thermoelectrics with Quantum Hall Edge States, *Phys. Rev. Lett.* **114**, 146801 (2015).
- [65] D. Sanchez and L. Serra, Thermoelectric transport of mesoscopic conductors coupled to voltage and thermal probes, *Phys. Rev. B* **84**, 201307(R) (2011).